Journal of
Marine Science and Engineering

MDPI

Article

Design and Computational Modelling of AUV Tunnel Thruster Covers for Efficient Operation

Christopher McNeill [1], Zachary Cooper-Baldock [2,*] and Karl Sammut [2,*]

1 College of Science and Engineering, Flinders University, Adelaide 5042, Australia
2 Centre for Defence Engineering, Research and Training (CDERT), Flinders University, Adelaide 5042, Australia
* Correspondence: zachary.cooperbaldock@flinders.edu.au (Z.C.-B.); karl.sammut@flinders.edu.au (K.S.)

Abstract: Autonomous underwater vehicles have seen widespread adoption across industrial, scientific, and defence applications. They are typically utilized to perform oceanic mapping, surveillance, and inspection-type missions. Hovering AUVs, used for inspection applications, are over-actuated vehicles incorporating multiple thrusters to enable multiple degrees of freedom control at a low velocity. These vehicles, however, are extremely energy-limited, owing to their restrictive structural design that prohibits large batteries. This necessitates careful hydrodynamic design to best utilize this limited energy storage. Of particular importance are the hydrodynamic propulsion efficiencies of these vehicles. Whilst the external structure of AUV platforms is relatively well-defined and hydrodynamically optimized, one area has seen limited focus and optimization. This is the immediate surroundings of the propulsion geometry and housing. In this body of work, we propose an adaptation to the traditional through-body tunnel thruster geometry of an over-actuated AUV platform. The modification is the inclusion of a retractable internal thruster cover. Subsequently, a comparison is provided between a clean-hull AUV configuration, one with open through-body thrusters, and one fitted with the designed cover geometry. A comprehensive computational fluid dynamics analysis is then converged and assessed using the Reynolds-Averaged Navier–Stokes equations. The drag and local flow fields are determined, where the covers are found to reduce the drag coefficient and total drag of the AUV by 9.51%, primarily due to a reduction of 9.91% in the pressure drag. These findings highlight the increased operational efficiency of the cover geometry and support the adoption of such covers for energy-constrained AUVs.

Keywords: efficiency; drag; hydrodynamics; computational fluid dynamics; maritime autonomy

Citation: McNeill, C.; Cooper-Baldock, Z.; Sammut, K. Design and Computational Modelling of AUV Tunnel Thruster Covers for Efficient Operation. *J. Mar. Sci. Eng.* **2024**, *12*, 2021. https://doi.org/10.3390/jmse12112021

Academic Editor: Adelaida Garcia-Magariño

Received: 27 September 2024
Revised: 23 October 2024
Accepted: 5 November 2024
Published: 9 November 2024

1. Introduction

The demand for underwater robotics has grown rapidly in recent years, driven by a decreasing cost to entry. This has directly correlated with an increased adoption of autonomous underwater vehicles (AUVs) and remotely operated vehicles (ROVs) for deployment in underwater settings for commercial, military, and scientific purposes [1–3]. These vehicles have seen an increased adoption in defence for bathymetric surveys, intelligence, surveillance, and reconnaissance (ISR), mine countermeasure, anti-submarine warfare, and object inspection/identification [1]. Common scientific purposes include surveys of lakes, seas, and ocean floors using sensors to identify concentrated and microscopic life within them. Such applications drive the ever-increasing need for long-endurance AUVs capable of travelling further on their limited capacity [2].

There are two classes of AUV configuration, as follows: under-actuated and over-actuated [4]. An under-actuated AUV is only able to control itself in a restricted number of degrees of freedom, surge, pitch, yaw, and roll. They typically feature a steering fin-propeller arrangement at the stern of the vessel, with either a cross- or X-fin arrangement [4]. In relatively low-speed conditions, with insufficient water flow over the steering fins, the control effectiveness of such vehicles is further reduced [4]. In contrast, over-actuated platforms can control most, if not all, of their six degrees of freedom. These platforms use thrusters typically located in the bow and stern of the vehicle, enabling effective control, especially when the AUV is travelling too slowly for its steering fins to produce sufficient actuation authority [5].

The exact means of actuation for an AUV can be broadly broken into a propeller or thruster device, where each has distinctly different characteristics [6]. Propellers are often used for under-actuated vehicles and are most commonly fixed-pitch, variable-pitch, or ducted propellers. These are often selected and optimized for the efficient operation of the AUV at a given speed [7]. These designs can be very efficient for a specific speed and thrust level, making them ideal for long-ranging operations with limited variations in speed or thrust requirements [8]. These designs are sub-optimal for operations when the speed and thrust requirements are variable, often resulting in a higher energy expenditure in these environments. Variable-pitch propellers can be rotated from the hub to enable variations in blade pitch whilst in operation [9]. This provides more control over the generated thrust and is beneficial for AUVs that need to operate efficiently at various speeds or conduct a range of tasks [10]. However, these designs are heavy and have a much larger number of mechanical components, which take payload space away from an already constrained AUV [11].

Thrusters typically comprise propellers located within ducted structures, but with smaller effective blade areas than fixed-pitch and variable propellers. This reduced blade area is beneficial, as it decreases the size of the thruster when located within the AUV, enabling a larger AUV payload to be carried. There are several thruster variants, such as through-body [12], tunnel [13], azimuth [14], vectored [15], and waterjet [16,17]. Through-bodied thrusters are propellers located in tunnel geometries that sit within the body of the AUV. Often, these are used in yaw and pitch pairs to control the vertical and lateral movement of the AUV [18]. Tunnel thrusters are similar but are connected to longer structures that go through the body of the AUV and can be located in the yaw, pitch, or roll axes depending on the desired controllability [19].

Azimuth thrusters are also used in over-actuated platforms and are steerable thrusters that can rotate 360 degrees around an axis [20]. These configurations are optimal for platforms that require an exceptional manoeuvrability. These designs are significantly more complex, however, and can increase the drag of the vessel significantly, so are often used for low-speed designs. Vectored thrusters are essentially ducted thrusters fixed at specific orientations on the vehicle frame and used for precise navigation and hovering [9]. Waterjets are a variation to the propeller thruster design, and they utilize a pump to draw water into the vessel and expel it at a high speed through a nozzle to generate thrust [16,17]. Waterjets provide a smooth and quiet operation and have subsequently been used in sensitive defence applications where a reduction in noise is extremely desirable. These, however, are inefficient at low speeds in comparison to propellers, and tend to be utilized on surface vessels or large submersibles due to their complexity and power demand [16,17]. There is also ongoing research [21–24] on alternative propulsion systems such as biomimetic propulsion, which is inspired by the movement of fish and marine animals and seeks to copy the movements of fins and tails to propel vehicles forward [23]. These designs often require significant structural redesigns and actuation structures compared to the propellers of thruster designs [21].

Historically, these designs have all been open to the surrounding freestream of the vessel. This results in noise, cavitation, and increased drag. Various strategies have been explored to reduce hydrodynamic effects, such as locating tunnel thrusters in line with the vessel hull [25], using specially designed nacelles [26], and optimizing the hub structure of the thruster/propeller [27]. Existing studies on tunnel thrusters have solely focused on the hydrodynamic properties of external thrusters and have neglected to assess methods to reduce through-body thruster hydrodynamic effects. Through-body thrusters create large orifices within the hull of an AUV, corresponding to an increased drag during operation compared to clean-hull forms [4]. This is undesirable, as the energy exertion is increased for the total duration of the operation, and subsequently decreases the AUV's range.

2. Contribution

This research develops and assesses a novel mechanism for enabling through-body thrusters to be open to the freestream when desired but closed during long-distance cruise activities. Existing research pertaining to thruster design [28–34] has focused on the power consumption [28,30–32], inner geometric structure [28,33,34], and placement and orientation [29,31] of the thrusters instead of their hydrodynamic efficiency with respect to the AUV hull structure. Furthermore, AUV hydrodynamic efficiency research has primarily focused on the broader vehicle hydrodynamics [35], hull structure only [36], and the mass and balance performance [37,38].

The thruster geometry hydrodynamics are important to the overall performance of the vessel and warrant an investigation into the effectiveness of such a closure mechanism. The goal of this mechanism is to reduce the hydrodynamic cost of operation, increasing the range and energy efficiency of the AUV. To achieve this, an internal sliding cover that sits within the hull structure of the AUV is designed. This mechanism can be retracted when required, allowing flow through the thrusters, and closed during cruise to reduce the operating drag, increasing efficiency. To assess the reduction in hydrodynamic drag, a converged Reynolds-Averaged Navier–Stokes analysis is undertaken. This assessment provides analysis across a range of operating speeds, as well as providing a baseline (clean-hull) benchmark and a worst case (open-thruster) assessment.

3. Materials and Methods

To assess how effective the novel cover structure is, a multi-step process must be employed. The cover structure itself (Section 3.1), in addition to how it is incorporated into the hull, must be understood, after which, separate geometries (Section 3.2) can be created for assessment. The hydrodynamic phenomenon of interest (Section 3.3) should also be clearly defined, before the computational fluid dynamics model (Section 3.4) can be structured and validated against (Section 3.5) existing known data. This section covers these topics in more detail below.

3.1. Cover Geometry

When designing the physical cover of the AUV thruster tunnels, it is important to understand how such a mechanism should fit within the hull and how much space exists to actuate this mechanism. Figure 1 shows a side view of the stern section of an example over-actuated GRAALtech X300 AUV (GRAALtech, Genova, Italy) with a vertical (pitch/heave) and horizontal (yaw/sway) through-body tunnel thruster pair.

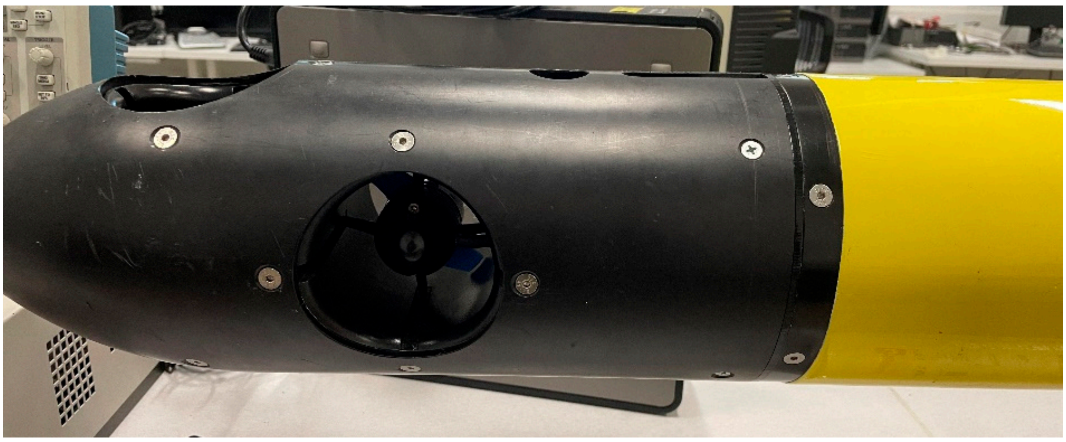

Figure 1. Side image of GRAALTech X300 AUV tail section showing a horizontal and vertical tunnel thruster pair.

To cover the thruster tunnel entrances, it is proposed that two separate mechanisms are located in each horizontal–vertical pair of tunnels. This ensures that if a single axis (yaw and pitch) is desired to operate, its individual cover can be retracted. The internal cover mechanism is provided in Figure 2, showing the open face (left) and closed tunnel (right) that can be alternated when the mechanism is pushed or pulled from the right-hand side.

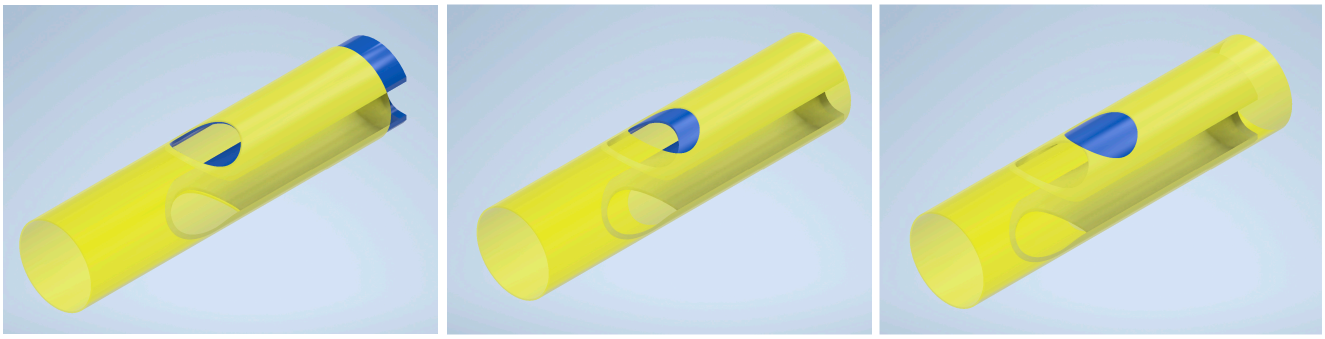

(**a**) (**b**) (**c**)

Figure 2. Pitch–axis tunnel thruster cover geometry shown. AUV outer hull indicated in yellow, internal sliding cover mechanism indicated in blue. Shown is the open (**a**), partially open (**b**), and closed (**c**) positions. Openings are provided for tunnel thruster operation when in the extended position, shown as the circular holes in the upper and lower facias of the section.

3.2. AUV Body Geometries

Three variations of the AUV vehicle geometry will be hydrodynamically assessed. These are the clean hull, open-tunnel hull, and the covered-tunnel hull. These are provided in Figures 3–5. The clean hull, as depicted in Figure 3, is a thruster-free hull, presenting the under-actuated baseline. This geometry is anticipated to have the lowest drag coefficient and drag force due to the lack of physical openings through the hull structure, resulting in a more efficient hydrodynamic profile. Figure 4 provides the open-tunnel hull, containing open passages where the through-body pitch and yaw thruster pairs will be located. These openings are present at the bow and the stern, as shown. Figure 5 presents the covered-tunnel variation. The hull structure is the same as the thruster body of Figure 4, but contains a recessed thruster cover in both the bow and stern pitch and yaw thruster pairs. The thruster cover is recessed below the outer hull by 3 mm. The thruster covers can be retracted by sliding them internally along the hull to uncover the thruster openings. The dimensions of the AUV are provided in Table 1 below.

Table 1. Dimensions of the AUV platform's length, diameter, tunnel diameter, and wetted area. Values are provided for all three geometries and indicate to which they belong.

Variable	Sizing [Unit]
AUV length	2.000 [m]
AUV diameter	0.110 [m]
Tunnel diameter	0.076 [m]
Tunnel cover depth	0.003 [m]
Wetted area (reference)	0.701 [m^2]
Wetted area (tunnel)	0.753 [m^2]
Wetted area (cover)	0.706 [m^2]

All variations of the AUV have a thruster, modelled as a propeller, without a shroud, located at the stern of the vessel, aft of the cross-fin structure. The propeller is based on a Blue Robotics T200 propeller, which is a commonly used thruster for small AUV platforms. The propeller will be modelled as an actuator disk [39], which will serve as a momentum source within the computational fluid dynamics model [40,41]. This is a reasonably accurate approximation of the flow field implications of a propeller, without resorting to a computationally demanding fully rotating mesh structure of a propeller. To develop an accurate model of the propeller, a tip speed profile and pressure jump profile must first be determined from T200 performance data [42].

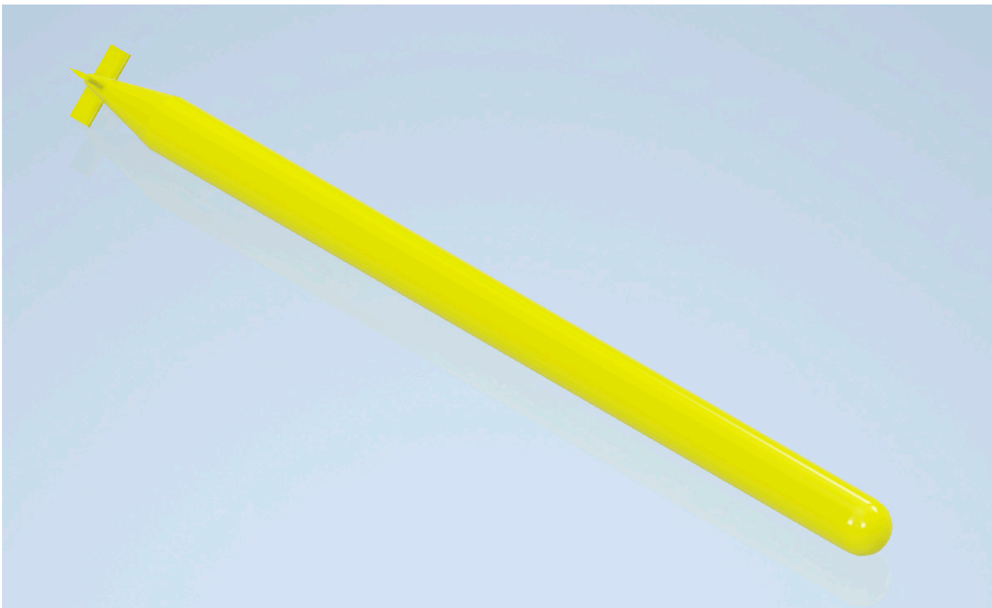

Figure 3. Reference (clean) hull geometric model of the AUV for computational modelling. Hull form is free of the thruster tunnels present on the cover and thruster models. A single Blue Robotics T200 propeller (BlueRobotics, Torrance, CA, USA) (not shown) is located at the stern of the vehicle, aft of the fin structure.

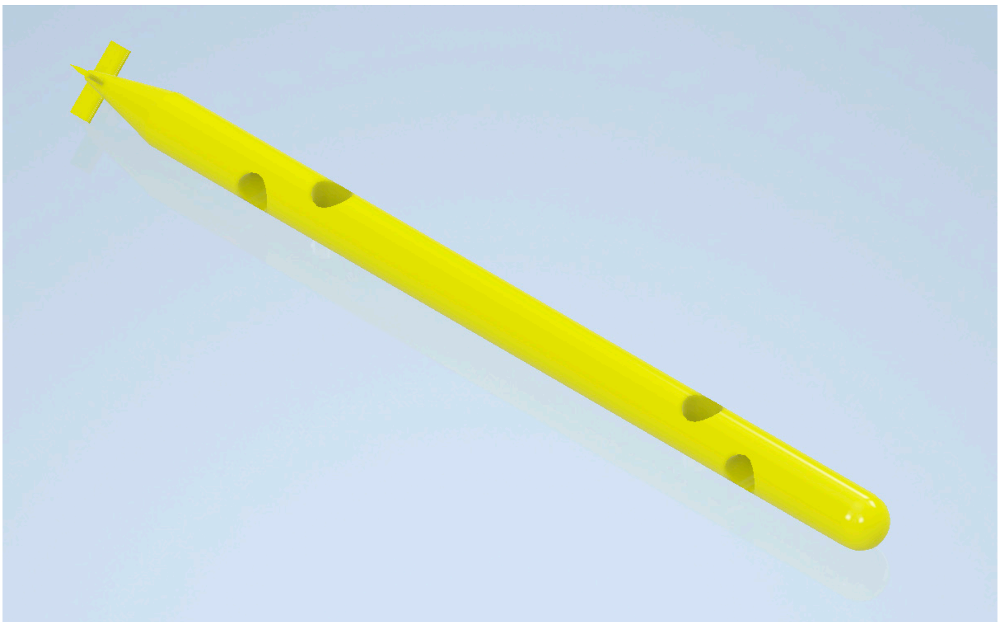

Figure 4. Open through-body tunnel thruster geometric model of the AUV for computational modelling. Hull form contains two pairs of through-body thrusters, each designed to actuate the vessel in the pitch/heave and yaw/sway axes. A single Blue Robotics T200 propeller is located at the stern of the vehicle (not shown), aft of the fin structure.

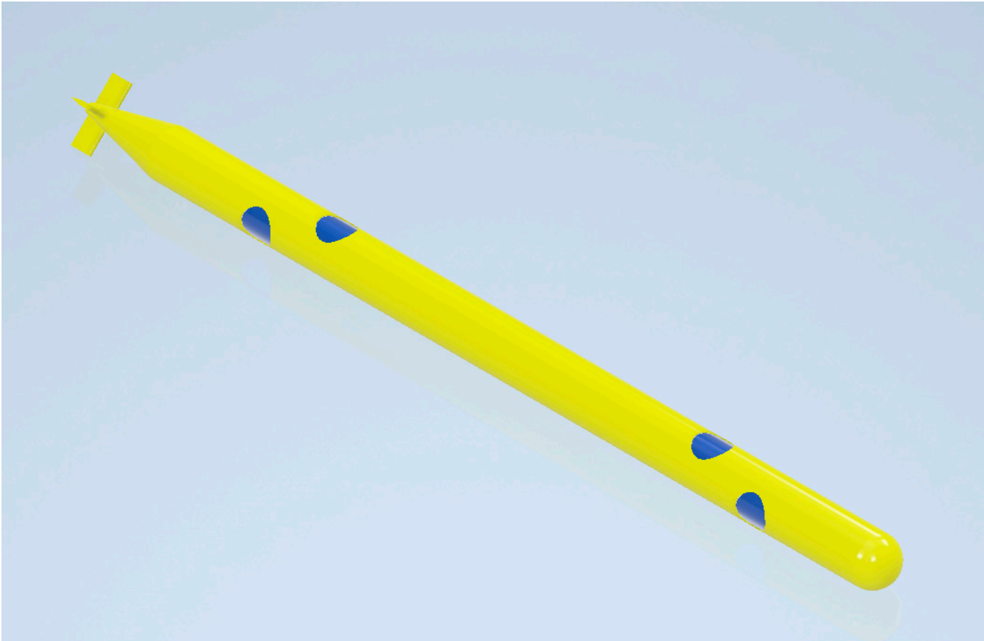

Figure 5. Closed through-body tunnel thruster geometric model of the AUV for computational modelling. Hull form contains two pairs of thrusters, each designed to actuate the vessel in the pitch/heave and yaw/sway axes. Sets of retractable covers (indicated in blue) are located at the stern and the bow, enabling the thruster tunnels to be sealed off from the freestream during forward motion, or retracted for thruster operation. A single Blue Robotics T200 propeller (not shown) is located at the stern of the vehicle, aft of the fin structure.

The assessment will be limited to a maximum speed of 2.50 m/s. The T200 has a maximum thrust force of 5.43 kgF at 2.50 m/s. This is a force of 53.21 N, which can be used to determine the required pressure jump by applying Equation (1), where the pressure (P) is determined by dividing the thrust (T) by the area of the propeller's rotational area (A). This yields the following:

$$P = \frac{T}{A} = \frac{53.21\ \mathrm{N}}{0.003279\ \mathrm{m}^2} = 16.23\ \mathrm{kPa}, \tag{1}$$

From the T200 performance data, it is also known that, at this speed and force, the motor pulse width modulation (PWM) value of the propeller, in microseconds, is 1850, and its maximum rotational RPM at this PWM is 3229 rpm. This, in conjunction with the propeller's diameter, can be used to determine the tip speed, in line with Equation (2). This equation relates the tip velocity (v_{tip}) to the outer diameter of the propeller (D_0) and the maximum rpm, as follows:

$$v_{tip} = \frac{\pi \cdot D_0 \cdot rpm}{60} = \frac{\pi(0.076)(3229)}{60} = 12.85\ \mathrm{m/s}, \tag{2}$$

This process is then repeated, using the T200 propeller performance data, for each speed under assessment in the hydrodynamic model, allowing for a dynamic tip speed and pressure jump to be incorporated into each simulation, depending on the flow speed under assessment. The full details of this are provided in Appendix A.

3.3. Hydrodynamic Phenomena of Interest

The primary indication of the cover's effectiveness will be the coefficient of drag recorded for each of the different speeds and configurations. The purpose of the cover is to decrease the drag coefficient of the thruster geometry, closer towards that of the clean-hull model. This reduction will come predominantly from an expected reduction in the drag force (F_D), which is a primary factor in the drag coefficient itself [41], as denoted by Equation (3), which relates the drag coefficient (C_D) to the force of drag (F), density (ρ), velocity (v), and the exposed area of the AUV (A_D).

$$C_D = \frac{2F_D}{\rho v^2 A_D} \tag{3}$$

3.4. Computational Fluid Dynamics Model

To execute the hydrodynamics assessment, a converged Reynolds-Averaged Navier–Stokes analysis was conducted. This assessment was undertaken using ANSYS Fluent 2023R1. The physical geometry of the AUV was located within a broad computational domain. The characteristic length (L) of the AUV was used to size the domain. The inlet was located 2L ahead of the AUV and the rear outlet was 5L behind the AUV, based on sizings in similar works [43–46], including propeller-based modelling work [46]. All side-facing outlets of the domain were located 2L away from the AUV. This separation distance ensured that boundary effects were minimized. Additionally, the following two sub regions were placed within the domain: the inner and the propeller region. These regions were used for local mesh cell size refinement to achieve the correct mesh sizings for the computational and turbulence model selected. These regions are depicted graphically in Figure 6.

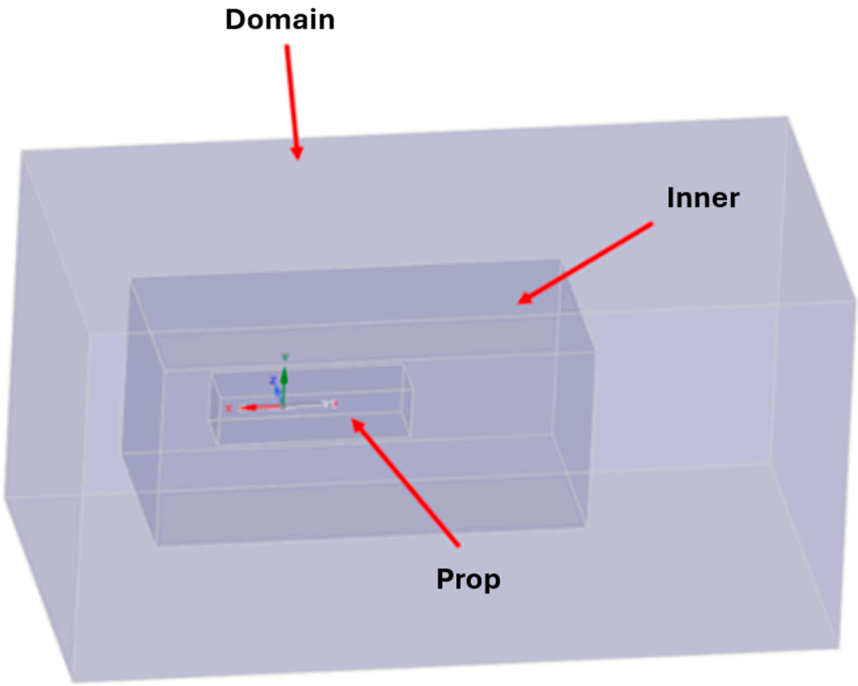

Figure 6. Computational domain of the assessment. Three different mesh sizing regions are used to control the mesh size and growth. The outer domain, inner domain, and the close (propeller) field. In the close field, the actuator disk (propeller) is shared with domain (indicated).

The propeller was modelled as an actuator disk. The tip profile, hub sizing, and effective blade area were defined within the computational model. This can be seen in Figure 7. The green area indicates the blade area, and the red propeller profile indicates that the boundary condition has been imposed within the computational model. This technique is often used in maritime CFD assessments reported in the literature [4,47]. It is this area (green) that will have the rotational profile of the propeller imposed, in addition to the pressure jump. This will produce an accurate estimation of the T200 flow field effects within the domain.

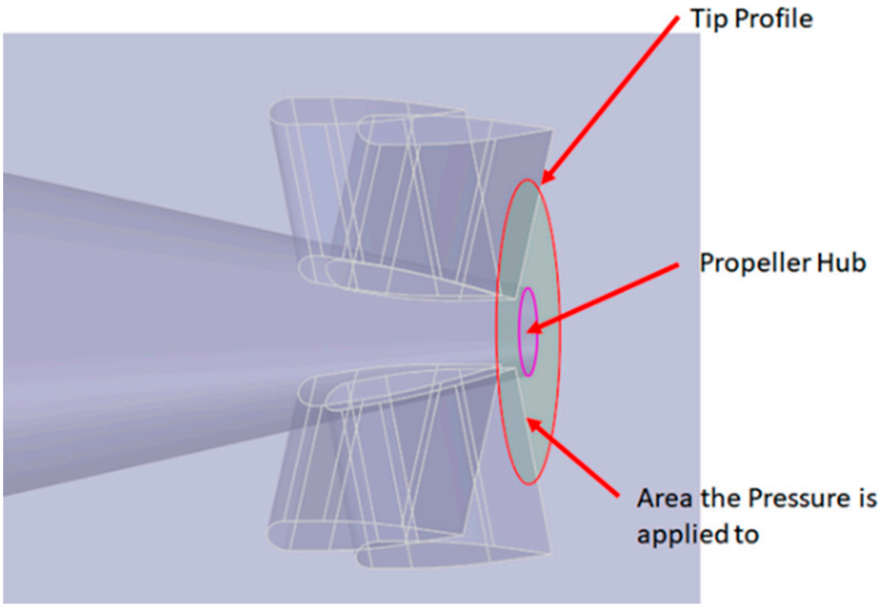

Figure 7. Propeller actuator disk model within the computational domain. The red profile outlines the tip of the propeller disk and the hub of the disk, while the green shaded area represents the blade area to which the pressure jump will be exerted. The tip region will be used to add the rotational velocity of the propeller into the domain, mimicking the function of the T200 propeller.

It is to this domain that the Reynolds-Averaged Navier–Stokes equations will be applied, in their incompressible isothermal RANS form, for Cartesian flow fields [48]. A steady approximation of these equations is used to decrease the computational requirements of full-body simulation at scale. This is an acceptable technique and also allows for the actuator disk propeller model to be used, instead of small-scale moving meshes of this region. The equations for the flow model are described by Equations (4) and (5) respectively. Equation (4) denotes the momentum equation and Equation (5) denotes the continuity equation. Within these, the variables used to denote the fluid density (ρ), mean velocity component in the i-th direction ($\overline{U_i}$) (m/s), time (t) (s), spatial coordinate in the j-th direction (x_j) (m), mean pressure (P) (Pa), dynamic viscosity of the fluid (μ) (Pa·s), Reynolds stress tensor components ($\overline{u_i' u_j'}$) (m^2/s^2) of the turbulent fluctuations, and body force per unit volume in the i-th direction (ρg_i) (N/m^3), which includes the gravitational force (g_i), are provided.

$$\rho\frac{\partial\overline{U_i}}{\partial t}+\rho\frac{\partial\overline{U_iU_j}}{\partial x_j}=-\frac{\partial P}{\partial x_i}+\frac{\partial}{\partial x_j}\left\{\mu\left(\frac{\partial\overline{U_i}}{\partial x_j}+\frac{\partial\overline{U_j}}{\partial x_i}\right)\right\}-\rho\frac{\partial\overline{u_i'u_j'}}{\partial x_j}+\rho g_i \tag{4}$$

$$\frac{\partial\overline{U_i}}{\partial x_i}=0 \tag{5}$$

Additionally, a turbulence model is required to approximate the turbulent changes to the flow. To address this, the realizable k-epsilon model is used, which has been developed for use in high-Reynolds-number flows [49]. The k-epsilon model provides closure to the RANS equations by modelling the Reynolds stress tensor using turbulent viscosity, which depends on k (turbulent kinetic energy) and ϵ (turbulent dissipation rate). The link is established through the Boussinesq eddy viscosity approximation that is given by Equation (6). This denotes the relation of the turbulent eddy viscosity μ_t, mean strain rate tensor S_{ij}, and Kronecker delta δ_{ij}.

$$\rho\frac{\partial\overline{u_i'u_j'}}{\partial x_j}=\frac{\partial}{\partial x_j}\left(2\mu_t S_{ij}-\frac{2}{3}\rho k\delta_{ij}\right) \tag{6}$$

The accuracy of this model, depending on the flow context, is reported to be between 97.91% and 99.23% when compared to experimental data [50]. Additionally, this turbulence model works well when pressure drag is being assessed, as it has a reported an accuracy of 96.96% [51]. The turbulence model is given by Equations (7) and (8), where the following symbols are employed: time (t), density (ρ), turbulent kinetic energy (k), position (x), velocity (u), viscosity (μ), Prandtl numbers for k and ϵ of (σ_k) and (σ_ϵ), respectively, the generation of TKE due to buoyancy (G_b), dissipation rate (ϵ), and fluctuating dilation in compressible turbulence to dissipation rate (Y_M), and user-defined source terms ($S_k,\ S_\epsilon$). Equation constants ($C_{1\epsilon},\ C_{2\epsilon},\ C_{3\epsilon}$) are also used.

$$\frac{\partial}{\partial t}(\rho k)+\frac{\partial}{\partial x_i}(\rho k u_i)=\frac{\partial}{\partial x_j}\left[\left(\mu+\frac{\mu_t}{\sigma_k}\right)\frac{\partial k}{\partial x_j}\right]+G_k+G_b-\rho\epsilon-Y_M+S_k \tag{7}$$

$$\frac{\partial}{\partial t}(\rho \epsilon)+\frac{\partial}{\partial x_i}(\rho \epsilon u_i)=\frac{\partial}{\partial x_j}\left[\left(\mu+\frac{\mu_t}{\sigma_\epsilon}\right)\frac{\partial \epsilon}{\partial x_j}\right]+C_{1\epsilon}\frac{\epsilon}{k}(G_k+C_{3\epsilon}G_b)-C_{2\epsilon}\rho\frac{\epsilon^2}{k}+S_\epsilon \tag{8}$$

The sublayer flow was bridged using empirical formulas [52] to determine the boundary conditions near the wall region, where the dimensionless thickness is described by Equation (9) and the dimensionless velocity by Equation (10). These equations are composed of density (ρ), distance from a setpoint to the wall (y_p), turbulent kinetic energy at the setpoint (k_p), and dynamic viscosity (μ). These formulations [52] are used to determine a target dimensionless wall thickness (y^+) that falls in the range from 30 to 300, which can be calculated via the application of Equations (11) and (12) below. Equation (11) relates the Reynolds length (Re_L) to the density (ρ), velocity (v), characteristic length (L), and dynamic viscosity (μ). In Equation (12), the first-layer mesh height (y_1) can be calculated from the target height (y^+), the characteristic length (L), and the Reynolds number.

$$y^+=\frac{\rho y_p C_\mu^{1/4} k_p^{1/2}}{\mu} \tag{9}$$

$$u^+=\frac{1}{k}\cdot\ln\left(Ey^+\right) \tag{10}$$

$$Re_L=\frac{\rho v L}{\mu} \tag{11}$$

$$y_1=L\cdot y^+\cdot\sqrt{80}\cdot Re_L^{-\frac{13}{14}} \tag{12}$$

3.5. Convergence and Validation

Once the mesh sizings in the initial layers were defined, mesh convergence was conducted across a range of fidelities. Four separate meshes were created, where their respective cell counts were increased from 400,000 to 16,000,000 cells. In order to determine the convergence, the drag force and coefficient of the AUV were recorded for each mesh. This allowed for the variation of both parameters to be determined as the fidelity of the mesh was increased. A target of less than 1.5% variation in the drag force and coefficient was used. This numerical variation was determined in relation to the original coarse mesh of 400,000 cells. The mesh parameters for each fidelity level are provided in Table 2. The numerical convergence of the drag force and coefficient is provided in Table 3. The convergence target of less than 1.5% variation was achieved at the highest mesh count of 16M cells, where a 1.15% variation was observed. This mesh was then used for the validation against existing studies and experiments.

Table 2. Meshing parameters for the cell count, viscous sublayer meshing, and the allowable maximum sizes for the domain, inner, and propeller defined regions of the computational space.

Mesh Cell Count	Inflation Layers	Maximum Allowable Cell Sizes		
		Domain	Inner	Propeller
465,197	15	0.500 [m]	0.150 [m]	0.040 [m]
1,012,565	15	0.500 [m]	0.100 [m]	0.035 [m]
7,184,031	15	0.500 [m]	0.030 [m]	0.012 [m]
16,214,647	15	0.500 [m]	0.030 [m]	0.010 [m]

Table 3. Numerical convergence analysis of mesh sizings with increasing cell count. Convergence was conducted at 2.5 m/s flow speed with a fixed set of propeller parameters for all models. The coarse (400k) cell model is used as the baseline for convergence. Cell count, drag coefficient, and convergence coefficient are provided.

Mesh Cell Count	Drag Force Fluctuation (ΔF_D)	Drag Coefficient Fluctuation (ΔC_D)
1,012,565	4.10%	4.10%
7,184,031	1.58%	1.58%
16,214,647	1.15%	1.15%

It is important to ensure that the converged computational fluid dynamics simulation adheres to both existing CFD experiments and experimental/tow tank correlations. In order to ensure this, two similar CFD works were used, where an AUV's hydrodynamic drag was assessed [47,53]. A third validation against the International Towing Tank Conference (ITTC) was also determined, this being the ITTC 1957 drag correlation [54]. Assessment was made at the converged numerical simulation Reynolds number of 1×10^6, where a drag coefficient (CD) of 0.151 was reported. The variation from [47] was 14.0%. and 2.80% from [53]. The ITTC-1957 correlation reported a CD of 0.165, resulting in a variation of 8.8%. These can be considered as minor fluctuations, due to the slight differences in the full form between this work and the existing work [47,53] and due to the approximate nature of the tow tank correlation [54]. From this close adherence to the pre-existing literature, the model was deemed to be sufficiently accurate.

4. Results

The following sub-sections present the results from various hydrodynamic parameter studies.

4.1. Drag Coefficients

Figure 8 displays the total drag coefficients recorded for the reference, covered-, and open-thruster geometries. It can be seen that these values are consistent with speed, as expected by the limited variation of the Reynolds number scheme [47,53]. The baseline reference geometry recorded a maximum drag coefficient of 0.150, with the covered-thruster tunnel incurring a 21.39% increase to a maximum of 0.182. The highest recorded drag coefficient was observed with the open-thruster geometry, which was 30.74% higher than the reference (0.195). Adopting the thruster cover at higher Reynolds numbers, such as at cruise, resulted in a drag coefficient reduction of 9.51%.

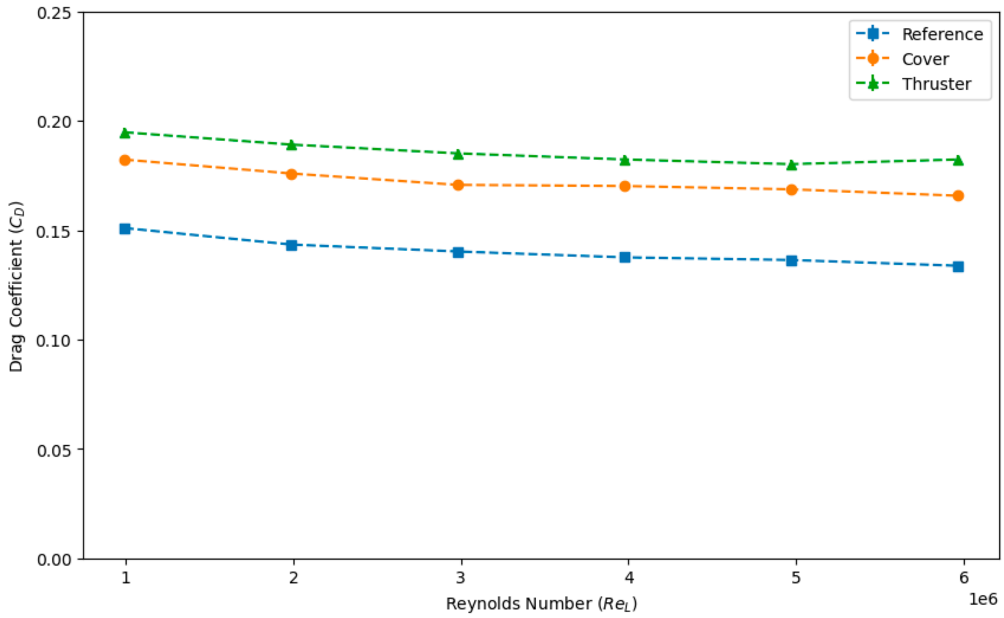

Figure 8. Drag coefficient (C_D) vs. Reynolds Number (Re_L) for the reference, covered-, and open-thruster configurations across the speed range [0.5, 0.5, 3.0] under assessment. Error bars are used to indicate a maximum 1.15% deviation of the RANS and realizable k-epsilon turbulence model used in the assessment.

4.2. Normalised Drag Forces

The normalised total drag forces are represented in Figure 9 below. It was again observed that the highest drag force and subsequent operating energy were exerted by the open-thruster configuration. The values presented are normalised against the highest recorded drag force of the open-thruster configuration. The disparity in the total drag force grew from 25.28% to 30.74% as the Reynolds number increased from 1×10^6 to 6×10^6. At the lowest speed, the covered-thruster geometry resulted in a 6.62% reduction in the drag force, increasing to a 9.51% difference at the fastest recorded speed. This is a significant reduction in operating drag via the adoption of a covered system, as it could directly correspond to a ~10% increase in the operational range of the vessel via the 9.51% increase in its efficiency.

Pressure drag, or form drag, is the dominating drag force exerted on the AUV during forward movements against the flow stream. This drag is due to the pressure difference between the bow and stern of the vessel. This drag acts directly on the forward area of the vessel, where the incoming flow is stagnated against the bow. This drag force increases with the square of velocity. A divergence in drag force with speed was observed to appear in relation to the covered- and open-thruster geometries when compared to the reference geometry as speed increased, as evidenced by Figure 9.

Again, the pressure drag was normalized against the highest recorded value from the high-speed open-thruster configuration. These data are presented in Figure 10. The cover system was found to reduce the pressure drag by 9.91% compared to the open-thruster configuration. However, the covered-thruster system still corresponded to a 22.45% higher drag than the reference configuration. There was a reduced benefit to the cover at a lower speed, which can be seen to correlate to a 6.96% reduction in pressured drag against the open-thruster model, whilst remaining 20.24% higher than the reference configuration's pressure drag.

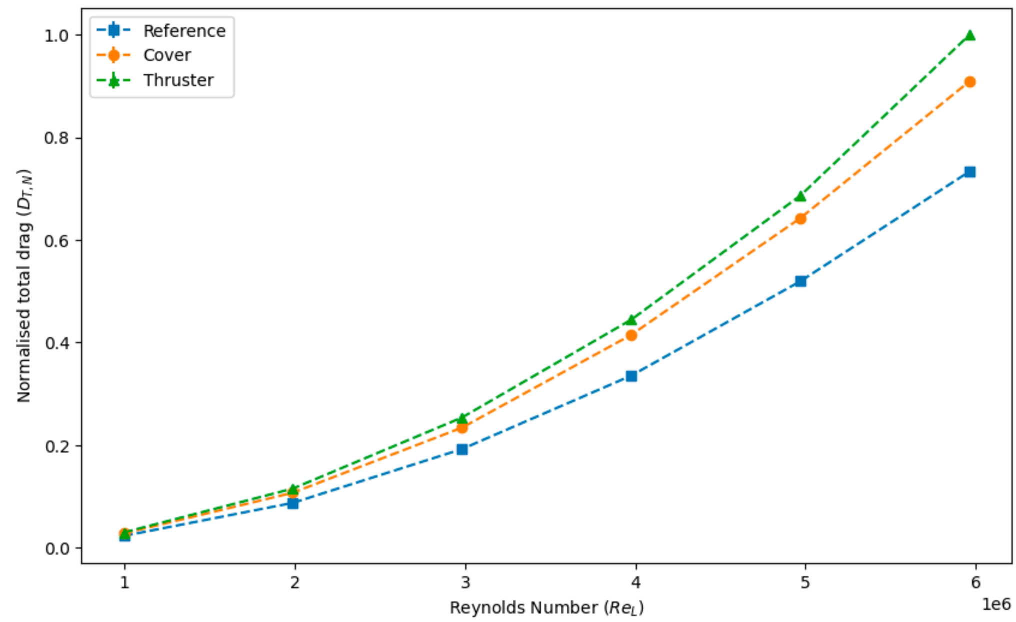

Figure 9. Normalized total drag (x, y, and z components), as reported for the reference, covered-, and open-thruster geometry configurations. Normalized drag force (D_{TN}) is presented, in accordance with the Reynolds Number (Re_L) of each speed assessed. All data are normalized against the highest recorded value from the open-thruster geometry.

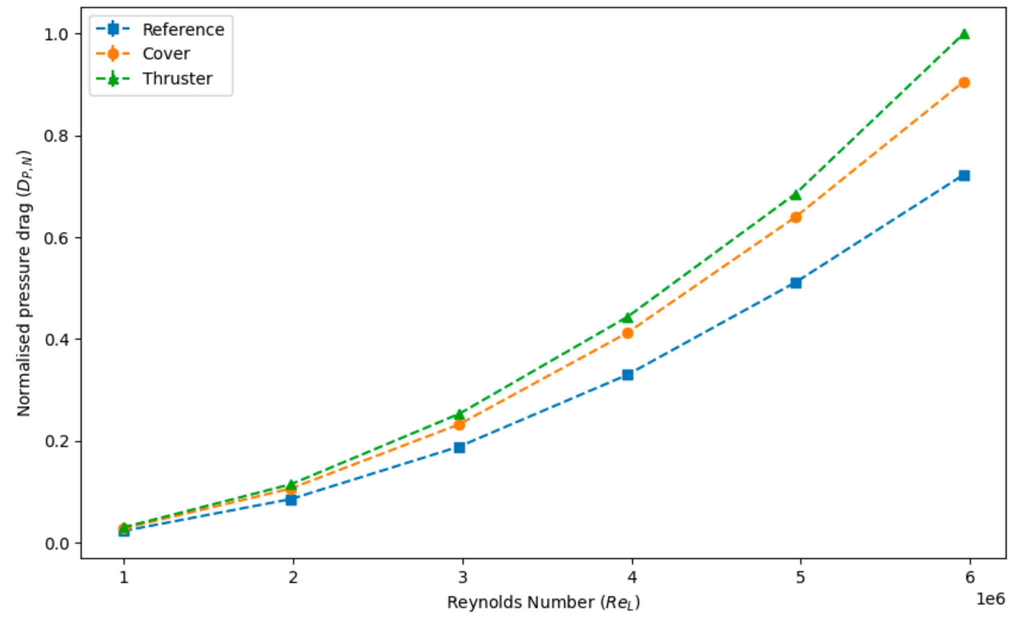

Figure 10. Normalized pressure drag (x, y, and z components), as reported for the reference, covered-, and open-thruster geometry configurations. Normalized pressure drag force (D_{PN}) is presented, in accordance with the Reynolds Number (Re_L) of each speed assessed. All data are normalized against the highest recorded value from the open-thruster geometry.

Viscous drag is caused by the friction between the AUV's surface geometry and the fluid flow. This arises due to the viscosity of the water as it flows along the hull. As the AUV moves forward, the hull experiences a shear force due to the velocity gradient in the boundary layer (viscous region). This is affected by velocity, surface geometry, and the exposed wetted area of the vessel. This drag is dominant at low speeds, with lessening impacts as the flow speed is increased. It was observed that the trends reported in the drag coefficient, total drag, and pressure drag were not replicated in the viscous drag.

Figure 11 details the normalized viscous drag experienced by the three configurations. The data were normalized against the maximum value recorded on the open-thruster model, which, unlike previous results, was not the maximum recorded value. It was observed that the highest viscous drag was exerted on the reference geometry, followed by the covered-thruster geometry, and that the least viscous drag was reported for the open-thruster configuration. At a high speed, the reference geometry was outperformed by the covered-thruster, configuration resulting in a 6.36% reduction in viscous drag. The open-thruster configuration was found to achieve a 10.06% lower viscous drag than the reference configuration and a 3.70% lower than the cover configuration. At a low speed, the differences between the recorded viscous drags across the three configurations were minimal. Again, the highest viscous drag was recorded for the clean reference model, with the cover reducing the viscous drag by 7.11% and the open configuration achieving a reduction of 9.75%.

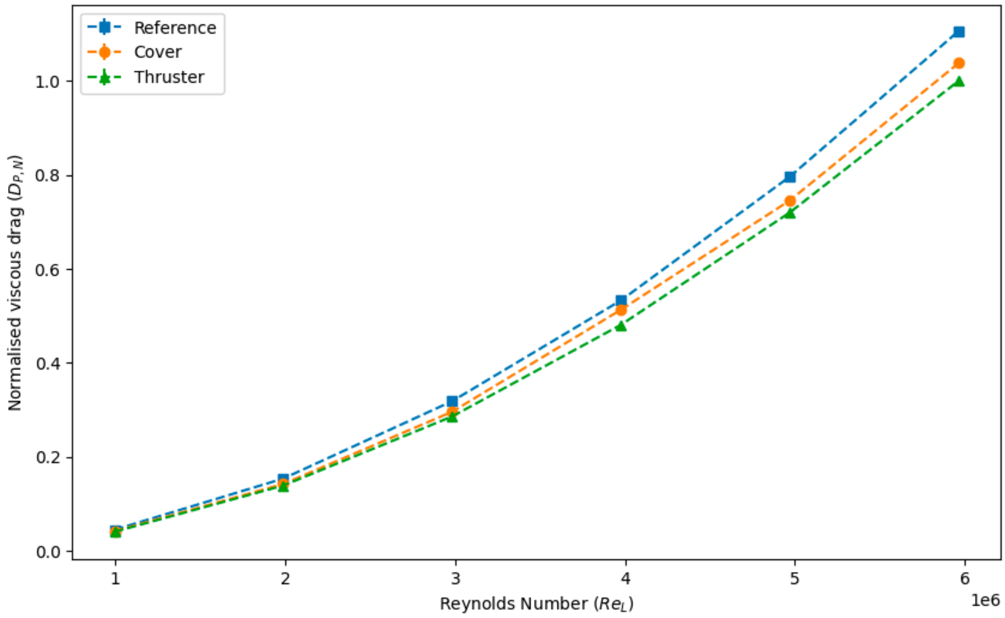

Figure 11. Normalized viscous drag (x, y, and z components), as reported for the reference, covered-, and open-thruster geometry configurations. Normalized viscous drag force (D_{VN}) is presented, in accordance with the Reynolds Number (Re_L) of each speed assessed. All data are normalized against the highest recorded value from the open-thruster geometry.

4.3. Flow Fields

Aside from the various drag properties, another factor of importance is the flow field immediately surrounding the AUV body, and particularly how this local flow field is modified by variations to the body geometry (reference, covered-thruster, and open-thruster configurations). The results for the flow-field study are presented in Figure 12. Also analysed were the flow field implications of shutting the rear vertical thruster cover while using the front thruster to actuate the pitch of the AUV. This secondary analysis, as provided by Figure 13, was achieved by modelling a second T200 thruster in an open-bow vertical tunnel and varying the angle of the incoming flow speed to simulate a pitch-up manoeuvre, whilst the rear vertical thruster contained a closed cover. The angle of this pitching manoeuvre was simulated from 0 degrees (horizontal) until a pitch of 30 degrees was achieved. During the pitch analysis, the flow through the tunnel geometry was assessed qualitatively for stall characteristics that may hinder the effective actuation of the AUV.

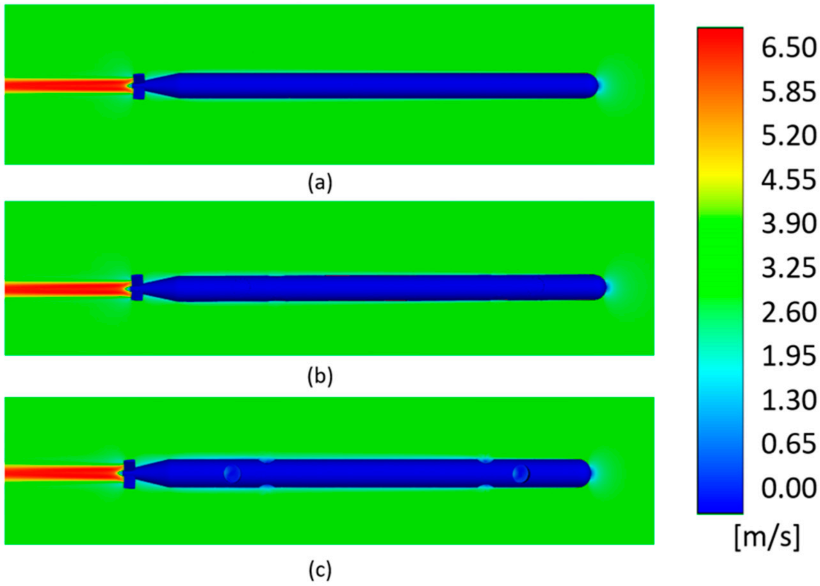

Figure 12. Local flow fields are shown on a vertical cross-section of the three different AUV body configurations. (**a**) Provides the reference geometric configuration, (**b**) the covered-thruster configuration, and (**c**) the open-thruster geometric configuration. Indicated right is the colour bar of velocity magnitude [m/s] for the 3.0 m/s flow speed case. Red indicates higher-velocity regions and blue indicates slow-velocity regions.

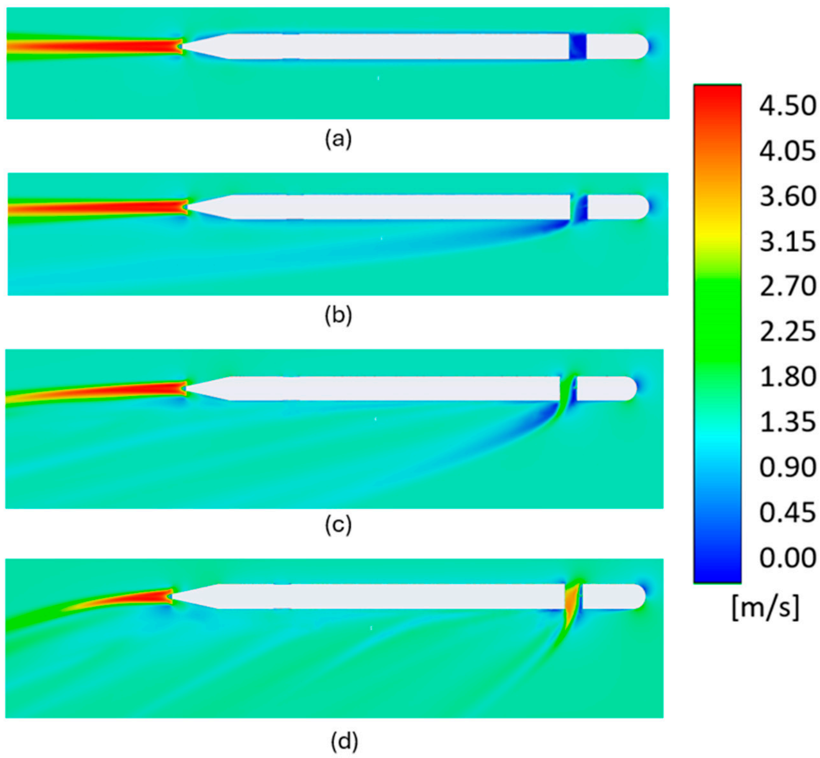

Figure 13. Local flow fields are shown on a vertical cross-section of the four different AUV pitching angle simulations. In all cases, the bow vertical thruster is open while the stern vertical thruster is closed. Provided are the flow field at a pitching angle of incidence of (**a**) 0 degrees, (**b**) 10 degrees, (**c**) 20 degrees, and (**d**) 30 degrees, pitching up. Indicated right is the colour bar of velocity magnitude [m/s] for the 3.0 m/s flow speed case. Red indicates higher-velocity regions and blue indicates slow-velocity regions.

The local flow field is found to vary minimally with variations to the body geometry, as evidenced by Figure 12. The local flow field on a vertical cross-section at a forward speed of 3.0 m/s is provided. It can be observed that there are differences in the wall-bounded flow region depending on the geometric configuration. The reference geometry (Figure 12a) sees almost no change in the viscous region around the body of the AUV, as expected for a smooth, hydrodynamically optimized vessel. Thruster covers, when in the closed position (Figure 12b), are observed to slow the flow field at the leading and trailing edge of the cover, where the 3 mm drop between the hull and the thruster cover geometry, as shown in Figure 2, occur. The impact of this appears minimal, with little disturbance to the velocity magnitude of the viscous layer. Finally, the open-thruster configuration (Figure 12c) is found to result in the most noticeable flow field disturbance due to the slow-moving fluid region contained within the open-thruster geometry. This region is still well-bounded by the boundary layer observed in Figure 12a,b, but is likely the cause of the adverse drag coefficient and drag forces for this configuration, when compared to the reference and covered geometries.

Figure 13 displays the flow field around the bow thruster model whilst the angle is incremented from 0 degrees to 30 degrees. When the angle of incoming flow is changed, modelling a pitching manoeuvre, the flow field through the bow thruster changes in response to its change in pitch. In level operation, at 0 degrees (Figure 13a), the flow field is uniform and constant within the bow thruster tunnel.

In this simulation, the forward vertical thruster is not operating, as it is not required to produce a pitching motion. When the angle is increased to 10 degrees (Figure 13b), a faster stream of flow enters the thruster housing due to the now-actuated tunnel thruster, but the blade wise distribution is not symmetrical, which may present operational challenges. At higher angles of attack, such as 20 degrees (Figure 13c) and 30 degrees (Figure 13d), the non-uniformity of the flow is reduced, where a more equal flow is drawn through the bow propeller, unlike the asymmetric flow exhibited in the 0-degree case (Figure 13a).

5. Discussion

This study investigated the potential of retractable thruster covers fitted to over-actuated AUVs to reduce drag effects and subsequently increase the hydrodynamic efficiencies of these vehicles for longer-range missions. As anticipated, the presence of open-thruster tunnels significantly increased the drag force and coefficient, and a beneficial reduction was observed via the adoption of covers, with the benefit increasing in proportion with the operating speed, as evidenced by Figures 8–11. The implementation of a cover mechanism was observed to reduce the drag coefficient (Figure 8) by 9.51%, with the pressure drag (Figure 10) being reduced by 9.91% and the viscous drag (Figure 11) by 6.36% at the maximum assessed vehicle speed. This correlated with a potential energy expenditure reduction of 10%.

The drag reduction primarily stemmed from the 9.91% decrease in pressure drag, indicating the benefits of the covered geometry with regard to streamlining the flow around the hull. The covers further produced minimized flow separation at the thruster geometries when the covers were employed, as shown in Figure 12b compared to Figure 12c. This method has been utilized before for the overall hull structure [55], but not directly for thruster openings, as reported here. Interestingly, while the covers were observed to reduce the pressure drag, they led to a marginal increase in the viscous drag compared to the open-thruster configuration at a higher speed. This indicates a potential trade-off between minimizing pressure and viscous drag in the covered design, where the maximum cruise speed of the AUV can be used to optimize either effect.

Additionally, it was observed that the total drag for the covered- and open-thruster geometries was higher than that for the clean reference configuration. This highlights the inherent trade-off between the manoeuvrability offered by the over-actuated configurations and the higher hydrodynamic efficiency of a clean-hull form. This aligns with the findings from studies exploring alternative propulsion systems and hull designs [25,26].

The flow field analysis provided further insight into the flow field effects of the cover, in comparison to the reference and open-thruster configurations. The cover was found to minimally affect the freestream flow and separation around the thruster geometry, particularly when compared to that of the open thrusters. However, further work could be performed to assess the effect of smoothing the step change between the covers and the outer hull form by tapering or chamfering the hull immediately around the thruster cover in order to reduce flow separation. Similar designs are known to be effective in other applications [56].

Examining the flow field during simulated pitching manoeuvres revealed an asymmetrical flow distribution through the bow thruster at lower angles of attack. This suggests potential challenges in achieving precise control at these angles [4] and emphasizes the need for further investigation into optimizing thruster control strategies when using covers during complex manoeuvres.

The findings from this study have important implications for the design and operation of energy-constrained AUVs. The demonstrated drag reduction achieved through retractable thruster covers translates to a potential increase in operational range, directly impacting mission endurance. While further research is necessary to optimize cover geometry and assess its impact on manoeuvrability, this study presents a compelling case for incorporating such covers into future AUV designs.

6. Conclusions

This study introduced a novel retractable thruster cover design aimed at improving the hydrodynamic efficiency of over-actuated AUVs. Through a comprehensive computational fluid dynamics (CFD) analysis, we demonstrated a 9.51% reduction in drag coefficient at higher speeds compared to an open-thruster configuration, primarily due to a 9.91% decrease in pressure drag. While viscous drag increased marginally, the overall drag reduction highlights the potential of this design to enhance the range and endurance of AUVs. Future research should focus on optimizing the cover geometry for minimal drag across all speeds, investigating the impacts of covers on manoeuvrability, and experimentally validating these findings. The successful implementation of retractable thruster covers could significantly benefit energy-constrained AUV applications by maximizing their operational efficiency and extending their mission capabilities.

Author Contributions: Conceptualization, C.M., Z.C.-B., and K.S.; methodology, C.M. and Z.C.-B.; validation, Z.C.-B.; formal analysis, C.M. and Z.C.-B.; investigation, C.M., Z.C.-B., and K.S.; data curation, C.M.; writing—original draft preparation, C.M. and Z.C.-B.; writing—review and editing, C.M., Z.C.-B., and K.S.; visualization, C.M.; supervision, Z.C.-B. and K.S. All authors have read and agreed to the published version of the manuscript.

Funding: This research received no external funding.

Data Availability Statement: The raw data supporting the conclusions of this article will be made available by the authors upon reasonable request.

Acknowledgments: This research was undertaken with the resources and services from Flinders University's High-Performance Computing platform DeepThought [https://doi.org/10.25957/FLINDERS.HPC.DEEPTHOUGHT], accessed 10 June 2024.

Conflicts of Interest: The authors declare no conflicts of interest.

Appendix A

This appendix contains the data used in the development of the propeller model within the computational fluid dynamics simulation, which was based on data provided by BlueRobotics [42] and the calculations outlined within the body text. Table A1 presents the speeds under assessment, force generated by the propeller, pressure jump over the propeller, rpm of the device, and subsequent tip speed.

Table A1. Actuator disk performance data used for the pressure jump and tip speed modelling within the ANSYS Fluent software package. Provided is the speed of the simulation (m/s), force (Kg·F), pressure (Pa), rpm, and tip speed (m/s).

Speed [m/s]	Force [Kg·F] [1]	Pressure [Pa]	RPM [1]	V_{tip} [m/s]
3.00	6.70	20,044	3907	15.55
2.50	5.43	16,236	3229	12.85
2.00	4.34	12,989	2651	10.55
1.50	3.26	9741	2074	8.25
1.00	2.17	6494	1496	5.96
0.50	1.09	3247	919	3.66

[1] Sourced from provided T200 BlueRobotics propeller data [42].

References

1. Bovio, D.C.E.; Baralli, F. Autonomous underwater vehicles for scientific and naval operations. *Annu. Rev. Control* **2006**, *30*, 117–130. [CrossRef]
2. Stefan, O.P.; Williams, B.; Steinberg, D.M.; Friedman, A.; Bryson, M. Reflections on a decade of autonomous underwater vehicles operations for marine survey at the Australian Centre for Field Robotics. *Annu. Rev. Control* **2016**, *42*, 117–130. [CrossRef]
3. Campbell, K.J.; Kinnear, S.; Thame, A. AUV technology for seabed characterization and geohazards assessment. *Lead. Edge* **2015**, *34*, 170–178. [CrossRef]
4. Cooper-Baldock, Z.; Santos, P.E.; Brinkworth, R.S.A.; Sammut, K. Payload bay berthing of underwater vehicles with a larger XLUUV. In Proceedings of the 7th Submarine Science Technology and Engineering Conference (SubSTEC7), Adelaide, Australia, 18–20 September 2023; Volume 1, pp. 97–104, ISBN 970-0-9944841-4-7.
5. Xiang, C.Y.X.; Zhang, Q.; Wilson, P.A.; Xu, G. Manoeuvring-based actuation evaluation of an AUV with control surfaces and through-body thrusters. *Appl. Ocean Res.* **2020**, *96*, 102046. [CrossRef]
6. Nicholson, J.W.; Healey, A.J. The present state of autonomous underwater vehicle (AUV) applications and technologies. *Mar. Technol. Soc. J.* **2008**, *42*, 1–124. [CrossRef]
7. Patil, P.V.; Khan, M.K.; Korulla, M.; Nagarajan, V.; Sha, O.P. Design optimization of an AUV for performing depth control maneuver. *Ocean Eng.* **2022**, *266*, 112929. [CrossRef]
8. Bellingham, J.G.; Zhang, Y.; Kerwin, J.E.; Erikson, J.; Hobson, B.; Kieft, B.; Godin, M.; McEwen, R.; Hoover, T.; Paul, J.; et al. Efficient propulsion for the Tethys long-range autonomous underwater vehicle. In Proceedings of the 2010 IEEE/OES Autonomous Underwater Vehicles, Monterey, CA, USA, 1–3 September 2010; pp. 1–7. [CrossRef]
9. Nagashima, Y.; Taguchi, N.; Ishimatsu, T.; Mizokami, T. Development of a Compact Autonomous Underwater Vehicle Using Variable Vector Propeller. In Proceedings of the 12th International Offshore and Polar Engineering Conference, Kitakyushu, Japan, 26–31 May 2002. ISOPE-I-02-176.
10. Du, X.; Cui, H.; Zhang, Z. Dynamics model and maneuverability of a novel AUV with a deflectable duct propeller. *Ocean Eng.* **2018**, *163*, 191–206. [CrossRef]
11. Stevenson, P.; Graham, D. Advanced materials and their influence on the structural design of AUVs. In *The Technology and Applications of Autonomous Underwater Vehicles*; Taylor & Francis: Abingdon, UK, 2003; pp. 77–91.
12. Steenson, L.V.; Phillips, A.B.; Furlong, M.; Rogers, E.; Turnock, S.R. Maneuvering of an over-actuated autonomous underwater vehicle using both through-body tunnel thrusters and control surfaces. In Proceedings of the 17th International Undersea Untethered Submersible Technology Conference, Portsmouth, NH, USA, 21–24 August 2011; Available online: https://nora.nerc.ac.uk/id/eprint/307875 (accessed on 15 September 2024).
13. Steenson, L.V.; Phillips, A.B.; Furlong, M.; Rogers, E.; Turnock, S.R. The performance of vertical tunnel thrusters on an autonomous underwater vehicle operating near the free surface in waves. In Proceedings of the Second International Symposium on Marine Propulsors, Hamburg, Germany, 15–17 June 2011; Available online: https://nora.nerc.ac.uk/id/eprint/307855 (accessed on 15 September 2024).
14. Eguchi, Y.Y.K.; Yasuda, S.; Awaya, I.; Adachi, T.; Yamauchi, Y. Low-speed and low-altitude AUV control. In Proceedings of the 2020 IEEE/OES Autonomous Underwater Vehicles Symposium, St. Johns, NL, Canada, 30 September–2 October 2020; pp. 1–5. [CrossRef]
15. Cavallo, E.; Michelini, R. A robotic equipment for the guidance of a vectored thruster AUV. In Proceedings of the 35th International Symposium on Robotics ISR, Paris, France, 23–26 March 2004; Volume 1, pp. 1–6.
16. Korde, U.A. Study of a jet-propulsion method for an underwater vehicle. *Ocean Eng.* **2004**, *31*, 1205–1218. [CrossRef]
17. Odetti, A.; Altosole, M.; Bruzzone, G.; Caccia, M.; Viviani, M. Design and Construction of a Modular Pump-Jet Thruster for Autonomous Surface Vehicle Operations in Extremely Shallow Water. *J. Mar. Sci. Eng.* **2019**, *7*, 222. [CrossRef]
18. Choi, J.-K.; Kondo, H. On fault-tolerant control of a hovering AUV with four horizontal and two vertical thrusters. In Proceedings of the OCEANS'10 IEEE SYDNEY, Sydney, NSW, Australia, 24–27 May 2010; pp. 1–6. [CrossRef]
19. Saunders, A.; Nahon, M. The effect of forward vehicle velocity on through-body AUV tunnel thruster performance. In Proceedings of the OCEANS'02 MTS/IEEE, Biloxi, MI, USA, 29–31 October 2002; pp. 250–259. [CrossRef]

20. Desai, M.; Halder, A.; Benedict, M.; Young, Y.L. A control scheme for 360° thrust vectoring of cycloidal propellers with forward speed. *Ocean Eng.* **2022**, *249*, 110833. [CrossRef]
21. Mazlan, A.; Naddi, A. A Fully Actuated Tail Propulsion System for a Biomimetic Autonomous Underwater Vehicle. Ph.D. Thesis, University of Glasgow, Glasgow, UK, 2015.
22. Bansal, P. Theoretical and Experimental Investigation of Magneto Hydrodynamic Propulsion for Ocean Vehicles. Master's Thesis, Virginia Polytechnic Institute and State University, Blacksburg, VA, USA, 2018.
23. Mojarrad, M. AUV biomimetic propulsion. In Proceedings of the OCEANS 2000 MTS/IEEE Conference and Exhibition, Providence, RI, USA, 11–14 September 2000; Volume 3, pp. 2141–2146. [CrossRef]
24. Matsumoto, M.; Kuwajima, Y.; Shigemune, H. Soft-skin actuator capable of seawater propulsion based on magnetohydrodynamics. In Proceedings of the 2022 IEEE/RSJ International Conference on Intelligent Robots and Systems (IROS), Kyoto, Japan, 23–27 October 2022; pp. 10059–10065. [CrossRef]
25. Kartidjo, M.W.; Manullang, R.A.M.; Jaya, A.S. Hydrodynamic design and analysis of low drag hybrid AUV-ITB. In Proceedings of the International Conference on Intelligent Unmanned Systems, Beijing, China, 27–29 August 2019.
26. Miller, L.M.; Njaka, T.; Brizzolara, S.; Curtin, T. Drag reduction and power optimization due to an innovative toroidal hull form of an AUV. In Proceedings of the International Workshop on Ship and Marine Hydrodynamics, Espoo, Finland, 28 August–1 September 2023; Volume 1288. [CrossRef]
27. D'Epagnier, K.P. AUV propellers: Optimal design and improving existing propellers for greater efficiency. In Proceedings of the OCEANS 2006, Boston, MA, USA, 18–21 September 2006; pp. 1–7. [CrossRef]
28. Gucer, C.A.; Acar, O.; Kantarcioglu, B.; Ulu, C. Thruster design for unmanned underwater vehicles. *J. Selcuk.-Tech.* **2020**, *19*, 196–208.
29. Krishnan, A.K.S.; Kadiyam, J.; Mohan, S. Comparative performance investigations of the intervention-class underwater vehicle with different possible thruster configurations using eight identical thrusters. *Ocean. Eng.* **2023**, *288*, 116147. [CrossRef]
30. Xu, D.; Yan, Z.; Xie, H.; Lu, L.; Xiao, Z.; Han, B. Demand-driven optimization method for thruster configuration of underwater vehicles considering capability boundary and system efficiency. *Ocean. Eng.* **2024**, *310*, 118749. [CrossRef]
31. Gasparoto, H.F.; Chocron, O.; Benbouzid, M.; Meirelles, P.S. Advances in reconfigurable vectorial thrusters for adapative underwater robots. *J. Mar. Sci. Eng.* **2021**, *9*, 170. [CrossRef]
32. Li, C.; Guo, S.; Guo, J. Performance Evaluation of a hybrid thruster for spherical underwater robots. *IEEE Trans. Instrum. Meas.* **2022**, *71*, 7503110. [CrossRef]
33. Li, S.; Chu, Z. Structural design of thruster for deep-sea underwater vehicle. *Int. Core J. Eng.* **2022**, *8*, 547–553. [CrossRef]
34. Liu, T.; Hu, Y.; Xu, H. Investigation of an underwater vectored thruster based on 3RPS parallel manipulator. *Math. Probl. Eng.* **2020**, *2020*, 9287241. [CrossRef]
35. Panda, J.P.; Mitra, A.; Warrior, H.V. A review on the hydrodynamic characteristics of autonomous underwater vehicles. *Proc. Inst. Mech. Eng. Part M J. Eng. Marit. Environ.* **2020**, *235*, 1. [CrossRef]
36. Luo, W.; Guo, X.; Dai, J.; Rao, T. Hull optimization of an underwater vehicle based on dynamic surrogate model. *Ocean Eng.* **2021**, *230*, 109050. [CrossRef]
37. Hou, S.; Zhang, Z.; Lian, H.; Xing, X.; Gong, X.; Xu, X. Hull shape optimization of small underwater vehicle based on kriging-based response surface method and multi-objective optimization algorithm. *Brodogr. Int. J. Nav. Archit. Ocean Eng. Res. Dev.* **2022**, *73*, 3. [CrossRef]
38. Lin, G.; Yang, Y.; He, Z.; Jiao, P. Hydrodynamic optimization in high-acceleration underwater motions using added-mass coefficient. *Ocean Eng.* **2022**, *263*, 112274. [CrossRef]
39. Lavimi, R.; Le Hocine, A.E.B.; Poncet, S.; Marcos, B.; Panneton, R. Hull shape optimization of autonomous underwater vehicles using a fully turbulent continuous adjoint solver. *Ocean Eng.* **2024**, *312*, 119256. [CrossRef]
40. Bontempo, R.; Cardone, M.; Manna, M.; Vorraro, G. A comparison of nonlinear actuator disk methods for the performance analysis of ducted marine propellers. *Proc. Inst. Mech. Eng. Part A J. Power Energy* **2015**, *229*, 539–548. [CrossRef]
41. Bontempo, R.; Manna, M. Actuator disc methods for open propellers: Assessments of numerical methods. *Eng. Appl. Comput. Fluid Mech.* **2016**, *11*, 42–53. [CrossRef]
42. BlueRobotics, T200 Public Performance Data. Available online: https://bluerobotics.com/store/thrusters/t100-t200-thrusters/t200-thruster-r2-rp/ (accessed on 10 June 2024).
43. Sadraey, M.; Müller, D. Drag force and drag coefficient. In *Aircraft Performance Analysis*; College of Engineering, Technology and Aeronautics, Southern New Hampshire University: Hooksett, NH, USA, 2009; Chapter 3.
44. Zaidi, M.; Taiar, R.; Polidori, G. Turbulence model choice for the calculation of drag forces when using the CFD method. *J. Biomech.* **2010**, *43*, 405–411. [CrossRef]
45. Abdellah, E.; Bo, W. CFD analysis on effect of front windshield angle on aerodynamic drag. *Mater. Sci. Eng.* **2017**, *231*, 012173. [CrossRef]
46. Hartwanger, D.; Horvat, A. 3D modelling of a wind turbine using CFD. In Proceedings of the NAFEMS Conference, UK, Cheltenham, UK, 10–11 June 2008.
47. Cooper-Baldock, Z.; Santos, P.E.; Brinkworth, R.S.A.; Sammut, K. Hydrodynamic analysis of payload bay berthing for underwater vehicles. *IEEE J. Ocean Eng.* **2024**, *49*, 727–748. [CrossRef]
48. Alfonsi, G. Reynolds-averaged Navier-Stokes equations for turbulence modelling. *Appl. Mech. Rev.* **2009**, *62*, 4. [CrossRef]

49. Shih, T.H.; Liou, W.W.; Shabbir, A.; Yang, Z.; Zhu, J. A new k-e eddy viscosity model for high Reynolds number turbulent flows—Model development and validation. *Comput. Fluids* **1995**, *24*, 227–238. [CrossRef]
50. Pan, Y.C.; Zhang, H.X.; Zhou, Q.D. Numerical prediction of submarine hydrodynamic coefficients using CFD simulation. *J. Hydrodyn.* **2012**, *24*, 840–847. [CrossRef]
51. Phillips, A.B.; Turnock, S.R.; Furlong, M. Influence of turbulence closure models on the vortical flow field around a submarine body undergoing steady drift. *J. Mar. Sci. Technol.* **2010**, *15*, 201–217. [CrossRef]
52. University of Washington, Modelling Turbulence. 2006. Available online: https://courses.washington.edu/mengr544/handouts-10/Fluent-k-epsilon.pdf (accessed on 16 June 2024).
53. Joung, T.H.; Sammut, K.; He, F.; Lee, S.K. Shape optimization of an autonomous underwater vehicle with a ducted propeller using computational fluid dynamics analysis. *Int. J. Naval Archit. Ocean Eng.* **2012**, *4*, 44–56. [CrossRef]
54. International Towing Tank Conference. ITTC—Recommended Procedures and Guidelines: Resistance Test. 7.5-02-02-01. 2011. Revision 3, pp. 1–13. Available online: https://ittc.info/media/1217/75-02-02-01.pdf (accessed on 15 September 2024).
55. Hai, H.; Zexing, Z.; Jiyong, L.; Qirong, T.; Wanli, Z.; Wang, G. Investigation on the mechanical design and manipulation hydrodynamics for a small sized, single body and streamlined I-AUV. *Ocean Eng.* **2019**, *186*, 1–13. [CrossRef]
56. Penkov, I.; Aleksandrov, D. Propeller shrouding influence on lift force of mini unmanned quadcopter. *Int. J. Automot. Mech. Eng.* **2017**, *14*, 4486–4495. [CrossRef]